Inorganic Chemistry
Cite This: Inorg. Chem. 2019, 58, 12385−12394
Article
pubs.acs.org/IC

# Unraveling Gibbsite Transformation Pathways into LiAl-LDH in Concentrated Lithium Hydroxide

Trent R. Graham,*[,†,‡] Jian Zhi Hu,[†,§,∥] Xin Zhang,[†] Mateusz Dembowski,[†] Nicholas R. Jaegers,[†,§,∥] Chuan Wan,[§] Mark Bowden,[†,⊥] Andrew S. Lipton,[⊥] Andrew R. Felmy,[†] Sue B. Clark,[○,#,▽] Kevin M. Rosso,[†] and Carolyn I. Pearce*[,○]

[†]Physical and Computational Sciences Directorate, Pacific Northwest National Laboratory, Richland, Washington 99354, United States
[‡]The Voiland School of Chemical and Biological Engineering, Washington State University, Pullman, Washington 99164, United States
[§]Institute for Integrated Catalysis, Pacific Northwest National Laboratory, Richland, Washington 99354, United States
[∥]Biological Science Directorate, Pacific Northwest National Laboratory, Richland, Washington 99354, United States
[⊥]Environmental Molecular Sciences Laboratory, Pacific Northwest National Laboratory, Richland, Washington 99354, United States
[#]Department of Chemistry, Washington State University, Pullman, Washington 99164, United States
[▽]Materials Science and Engineering Program, Washington State University, Pullman, Washington 99164, United States
[○]Energy and Environment Directorate, Pacific Northwest National Laboratory, Richland, Washington 99354, United States

Supporting Information

**ABSTRACT:** Gibbsite ($\alpha$-$Al(OH)_3$) transformation into layered double hydroxides, such as lithium aluminum hydroxide dihydrate (LiAl-LDH), is generally thought to occur by solid-state intercalation of $Li^+$, in part because of the intrinsic structural similarities in the quasi-2D octahedral $Al^{3+}$ frameworks of these two materials. However, in caustic environments where gibbsite solubility is high relative to LiAl-LDH, a dissolution-reprecipitation pathway is conceptually enabled, proceeding via precipitation of tetrahedral ($T_d$) aluminate anions ($Al(OH)_4^-$) at concentrations held below 150 mM by rapid LiAl-LDH nucleation and growth. In this case, the relative importance of solid-state versus solution pathways is unknown because it requires *in situ* techniques that can distinguish $Al^{3+}$ in solution and in the solid phase (gibbsite and LiAl-LDH), simultaneously. Here, we examine this transformation in partially deuterated LiOH solutions, using multinuclear, magic angle spinning, and high field nuclear magnetic resonance spectroscopy ($^{27}Al$ and $^{6}Li$ MAS NMR), with supporting X-ray diffraction and scanning electron microscopy. *In situ* $^{27}Al$ MAS NMR captured the emergence and decline of metastable aluminate ions, consistent with dissolution of gibbsite and formation of LiAl-LDH by precipitation. High field, *ex situ* $^{6}Li$ NMR of the the progressively reacted solids resolved an $O_h$ $Li^+$ resonance that narrowed during the transformation. This is likely due to increasing local order in LiAl-LDH, correlating well with observations in high field, *ex situ* $^{27}Al$ MAS NMR spectra, where a comparatively narrow LiAl-LDH $O_h$ $^{27}Al$ resonance emerges upfield of gibbsite resonances. No intermediate pentahedral $Al^{3+}$ is resolvable. Quantification of aluminate ion concentrations suggests a prominent role for the solution pathway in this system, a finding that could help improve strategies for manipulating $Al^{3+}$ concentrations in complex caustic waste streams, such as those being proposed to treat the high-level nuclear waste stored at the U.S. Department of Energy's Hanford Nuclear Reservation in Washington State, USA.

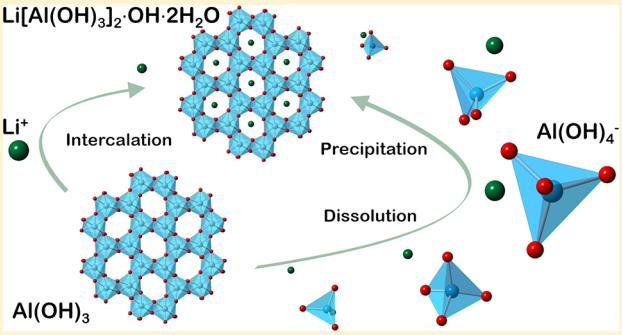


## 1. INTRODUCTION

Clay-like hydrotalcite materials, commonly known as layered double hydroxides (LDHs), are composed of quasi two-dimensional metal hydroxide sheets that are typically bound together by interlayer anions. LDH materials are widely used in ion separations,[1−4] drug delivery,[5] corrosion inhibition,[6−8] carbon dioxide sorption,[9] and catalysis.[10−12] LDH materials that cointercalate cations[13] and anions[14] are also possible, with high selectivity, e.g., $Li^+ \gg Ni^{2+} \gg Co^{2+} \approx Zn^{2+}$. Most LDH materials can be represented by the general formula $[M_{1-x}^{z+}M_x^{3+}(OH)_2]^{y+}(A^{n-})_{y/n}\cdot mH_2O$, where usually $z = 2$ and $y = x$.[15] Generally, partial replacement of divalent metal cations by trivalent ions is charge-compensated by anions in the interlayer region, and selection of these metal ions and interlayer anions imparts tunable properties.[16,17] Distinct from

Received: July 5, 2019
Published: September 5, 2019






DOI: 10.1021/acs.inorgchem.9b02000
Inorg. Chem. 2019, 58, 12385−12394

the formation of LDH by partial replacement of divalent metal cations, $Li^+$ intercalation into the octahedral vacancies in aluminum hydroxides (i.e., gibbsite and bayerite) also corresponds with intercalation of charge balancing, hydrated anions into the interlayer region to form lithium aluminate based LDH.[18] For example, in lithium hydroxide solutions, gibbsite ($\alpha$-$Al(OH)_3$) transforms into lithium dialuminate hydroxide dihydrate (LiAl-LDH, $Li[Al(OH)_3)]_2OH{\cdot}2H_2O$).[19,20]

LiAl-LDH is an important precursor of lithium aluminate ($LiAlO_2$), which is widely used in energy applications including tritium production,[21,22] fuel cells,[23] and lithium batteries.[24] LiAl-LDH precipitation in caustic solutions has also been proposed as a strategy to control $Al^{3+}$ concentrations in $Al^{3+}$-rich radioactive high-level nuclear wastes (HLW) for processing into more stable glass wasteforms.[25,26] Large quantities of this waste are located at Department of Energy (DOE) sites such as Hanford, Washington, USA, where the predominant $Al^{3+}$ phase is gibbsite ($\alpha$-$Al(OH)_3$) coexisting with high concentrations of soluble aluminate ions ($Al(OH)_4^-$).[27] At such sites, the efficiency of HLW stabilization through vitrification can be greatly improved by reducing the concentration of $Al^{3+}$ in the waste stream, enabling increased waste loading in the glass.[25,26] $Li^+$ addition is motivated by two factors: $Al^{3+}$ solubility in $Li^+$-rich caustic electrolytes is low compared to NaOH solutions (e.g., ca. 10 mM in 3 M LiOH versus ca. 200 mM in 3 M NaOH[28]), and the nucleation of the solubility limiting LiAl-LDH phase is kinetically facile, relative to the kinetic bottlenecks typically encountered with pure $Al^{3+}$ hydroxide phases such as gibbsite.[29] The present study is motivated by the need to better understand the competition between various possible pathways to LiAl-LDH in caustic aluminum-bearing aqueous solutions.

Multiple pathways to LiAl-LDH exist in $Li^+$ solutions where gibbsite and aluminate ions are present simultaneously: (i) solid-state transformation of gibbsite by intercalation of $Li^+$ cations and (ii) precipitation via aluminate ions originating from the dissolution of gibbsite.[19,29] The dissolution/reprecipitation process is conceptually competitive at temperatures lower than typical synthesis conditions (90 °C).[18] Relevant dissolution/reprecipitation equilibria can be summarized by the following two reactions:

$$Al(OH)_3(s) + OH^-(aq) \rightleftharpoons Al(OH)_4^-(aq) \quad (1)$$

$$2Al(OH)_4^-(aq) + Li^+(aq) + 2H_2O(aq) \rightleftharpoons (Li[Al(OH)_3]_2OH{\cdot}2H_2O)(s) + OH^-(aq) \quad (2)$$

whereas the intercalation of $Li^+$ and $OH^-$ ions into gibbsite proceeds by

$$2Al(OH)_3(s) + Li^+(aq) + OH^-(aq) + 2H_2O(aq) \rightleftharpoons (Li[Al(OH)_3]_2OH{\cdot}2H_2O)(s) \quad (3)$$

Intercalation is a solid-state topotactic transformation pathway enabled by the close correspondence of gibbsite and LiAl-LDH structures. Crystallographic cavities in the structure of gibbsite are ideal for insertion of $Li^+$, and interlayer domains are readily accessible to counterions. In gibbsite (Figure 1A and B), layers of edge-sharing $Al^{3+}(OH)_6$ octahedra bound to each other through hydrogen bonding stack into a pseudohexagonal structure.[30] Within each layer, only two-thirds of the octahedral cavities created by close-packed oxygen layers are occupied by $Al^{3+}$; the remaining unoccupied cavities have a radius of approximately 0.7 Å, enabling insertion of $Li^+$, which has a radius of 0.68 Å.[31] To balance the charge, $Li^+$ insertion occurs concurrently with incorporation of anions such as $OH^-$, $NO_3^-$, $Cl^-$, or $CO_3^{2-}$ into the interlayer,[32] as shown in Figure 1C,D. This transformation increases the lattice constant between octahedral sheets (along the *c*-axis, Figure 1) from 9.74 Å in gibbsite to, for example, 14.30 or 14.95 Å in $Li[Al(OH)_3]_2Cl{\cdot}nH_2O$ or $Li[Al(OH)_3]_2Br{\cdot}nH_2O$, respectively.[33,34] The mechanism of $Li^+$ intercalation into gibbsite has been studied[13,14,18,19,35,36] but remains incompletely characterized. More generally, in the case of complex caustic solutions, the extent to which the transformation reaction proceeds via solution versus solid-state pathways, or a combination of the two, is not readily predictable over a wide range of conditions.

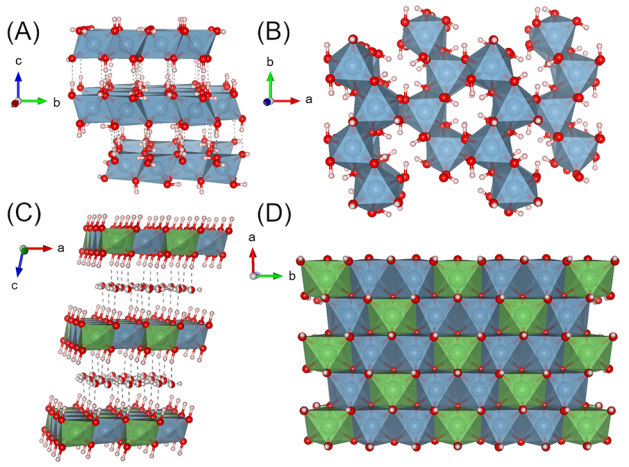


**Figure 1.** Crystal structure of gibbsite, $\alpha$-$Al(OH)_3$, and LiAl-LDH, $Li[Al(OH)_3)]_2OH{\cdot}2H_2O$. (A) The structure of gibbsite perpendicular to the *c* and *b* axes. (B) The structure of gibbsite perpendicular to the *b* and *a* axes. (C) The crystal structure of LiAl-LDH, perpendicular to the *a* and *c* axes where the half-filled, red/white spheres in the interstitial layers indicate half occupancy. (D) The crystal structure of LiAl-LDH perpendicular to the *a* and *b* axes. Aluminum, oxygen, lithium, and hydrogen atoms are blue, red, green, and white, respectively.

To close this knowledge gap, we examined the transformation pathways of gibbsite to LiAl-LDH by reaction with LiOH. Gibbsite dissolution in 3 M LiOH at concentrations above the equilibrium $Al^{3+}$ solubility limit (ca. 10 mM) was characterized using unique *in situ* MAS NMR techniques that are capable of resolving solid and liquid species simultaneously in alkaline solutions.[37] *In situ* $^{27}Al$ MAS NMR spectroscopy, unlike prior synchrotron X-ray scattering studies,[35,36] allows the tetrahedral aluminate ion concentration in solution to be determined, which can inform on the extent to which dissolution/reprecipitation processes are involved in the transformation (i.e., eqs 1−3). *Ex situ*, high field (20.0 T) $^6Li$ and $^{27}Al$ NMR measurements on the solid phases provided insight into the evolving LiAl-LDH structure during the transformation. NMR measurements were complemented by *ex situ* solids characterization by X-ray diffraction (XRD) and scanning electron microscopy (SEM). In addition to probing the transformation mechanism, understanding the aluminate ion concentration profile also provides insight into $Al^{3+}$ precipitation in alkaline media more generally, with relevance


DOI: 10.1021/acs.inorgchem.9b02000
Inorg. Chem. 2019, 58, 12385−12394

to applications including the preparation of catalysts, drug delivery devices, passivation material, and ion−ion exchangers.

## 2. MATERIALS AND EXPERIMENTAL PROCEDURES

**2.1. Synthesis of Gibbsite Nanoplates.** Euhedral, hexagonal gibbsite nanoplates were synthesized according to procedures described elsewhere.[38] A solution of 0.25 M aluminum nitrate ($Al(NO_3)_3{\cdot}9H_2O$, ≥ 98%, Sigma-Aldrich) in water (18 MΩ) was prepared and titrated using 1.0 M sodium hydroxide (NaOH ≥ 98%, Sigma-Aldrich) until a pH of 5 was attained. The precipitated gel dispersion was mixed for 1 h, collected by centrifugation, and redispersed in water three times to remove $Na^+$ and $NO_3^-$ ions. After decanting the third wash, the pelleted gel was dispersed in water (0.3 g pelleted gel per mL of water) and transferred to a 22 mL, Teflon lined, Parr vessel. The Parr vessel was heated in a rotary oven for 72 h at 80 °C and 10 rpm. The product was collected and washed by centrifugation, redispersed in water three times, and finally dried in an oven at 80 °C overnight.

Following the synthesis of gibbsite, all sample manipulation was conducted in a glovebox under a nitrogen ($N_2$) atmosphere to minimize carbon dioxide ($CO_2$) capture by the concentrated lithium hydroxide (LiOH) solution. A partially deuterated solution of 3 M LiOH (≥98%, Sigma Aldarich) in deuterium oxide ($D_2O$, ≥ 99%, Sigma Aldarich) was prepared. *Ex situ* XRD and NMR samples were prepared by dispersing gibbsite nanoplates (0.5 M $Al^{3+}$) in 3 M LiOH in $D_2O$ with vigorous mixing. At various sampling times, the solid phase was separated by centrifugation, washed three times with $D_2O$, and dried at ambient temperature.

**2.2. Nuclear Magnetic Resonance Spectroscopy.** *In situ* $^{27}Al$ MAS NMR was conducted on a Varian-Inova NMR spectrometer at a field strength of 7.0 T at a calibrated[39] temperature of 25 °C using a 7.5 mm MAS probe. The temperature was controlled by air flowing through the probe at 10 L/min. Samples were prepared by loading gibbsite into a 7.5 mm custom designed zirconia rotor.[37] A solution of 3 M LiOH in $D_2O$ was then added to create a 0.5 M $Al(OH)_3$ dispersion; the rotor was assembled and loaded into the NMR spectrometer. The sample spinning rate was approximately 3.8 kHz. $^{27}Al$ MAS NMR spectra were collected using a single pulse of 2.5 $\mu$s (corresponding to a liquid $\pi/4$ and solid $\pi/2$ pulse width, Supporting Information, Figure S1) and an 80 ms acquisition time. A recycle delay (d1) nutation experiment is shown in Figure S2. The $^{27}Al$ chemical shift was referenced externally to 1 M $Al(NO_3)_3$ in $H_2O$ ($\delta$ = 0 ppm). Spectra at 7.0 T were analyzed in Mestrenova (v10) where line broadening (20 Hz) was applied. In this work, due to the low spectral resolution and large number of $^{27}Al$ MAS NMR spectra at 7.0 T, Gaussian−Lorentzian lineshapes were utilized to conveniently estimate information regarding the $O_h$ central transition quadrupole broadening. In the case of highly disordered solids, the Czjzek model is typically used to analyze materials with different extents of disorder.[40]

*Ex situ*, high field $^6Li$ and $^{27}Al$ measurements were conducted on a Varian-Inova NMR spectrometer operating at 20.0 T at 25 °C with a spin rate of 20 kHz using a 3.2 mm commercial probe. The temperature was controlled by air flowing through the probe at 10 L/min. Both $^{27}Al$ and $^6Li$ NMR pulse sequences utilized a single, solid $\pi/4$ pulse (2.0 and 6.0 $\mu$s, respectively). A solid $\pi/4$ pulse was used because quadrupolar second order effects are reduced at 20.0 T, resulting in resonance behavior approaching that of spin 1/2 nuclei and was validated by the insensitivity of the resonance line shape of a mixture of LiAl-LDH and gibbsite to pulse width variation between ca. $\pi/20$ and $\pi/2$ tip angles (Figure S3). $^{27}Al$ chemical shifts were reported with respect to 1 M $Al(NO_3)_3$ in $H_2O$ ($\delta$ = 0 ppm), and $^6Li$ chemical shifts were referenced to 1 M LiCl in $H_2O$ ($\delta$ = 0 ppm). The recycle delay for $^{27}Al$ and $^6Li$ was 1 and 100 s, respectively. The acquisition time for $^{27}Al$ and $^6Li$ was 0.1000 and 0.2016 s, respectively. Typically, over 50 000 transients were collected for $^{27}Al$, while 512 transients were collected for $^6Li$. Spectra were processed in Mestrenova where 50 Hz line broadening was applied for $^{27}Al$ spectra and 25 Hz line broadening for $^6Li$ spectra at 20.0 T. DMFIT (release #20180327) was used to evaluate quadrupolar line shape parameters in the $^{27}Al$ MAS NMR spectra collected at 20.0 T. Second order, quadrupolar line shapes of the $^{27}Al$ MAS NMR central transitions were estimated with the Qmas 1/2 model, which assumes an infinite spinning rate. The quadrupolar coupling parameters and relative site distribution of the two Al sites in gibbsite were fixed, and the fewest additional sites were introduced to fit the $O_h$ region of the spectra. The fit spectra and quadrupolar coupling parameters are included in the Supporting Information. Gaussian line shape parameters for the $^6Li$ MAS NMR spectra were determined in Mestrenova.

**2.3. X-ray Diffraction.** XRD patterns were acquired on a Philips X'pert Multi-Purpose diffractometer (PANAlytical Almelo, The Netherlands), equipped with a fixed Cu anode operating at 40 mA and 50 kV. Harvested solids corresponding to *ex situ* $^{27}Al$ MAS NMR samples were loaded in a custom-built gas vessel equipped with a Kapton window in a glovebox filled with $N_2$. Phase identification was performed in JADE (v. 9.5.1, Materials Data Inc.) utilizing the 2012 PDF4+ database (International Center for Diffraction Data). Phase compositions were determined using a Pawley refinement in which the intensity of the XRD pattern of LiAl-LDH was referenced to a known mixture of LiAl-LDH and $TiO_2$ (Standard Reference Material, National Bureau of Standards, 674A). Refinements were conducted in TOPAS (v5) both with and without preferential orientation included in the refinement.

**2.4. Scanning Electron Microscopy.** A Helios NanoLab 600i SEM (FEI, Hillsboro, OR) was used to examine the harvested solids, gibbsite and LiAl-LDH, obtained following reaction in 3 M LiOH in $D_2O$. The samples were sputter coated with approximately 5 nm of carbon before imaging.

**2.5. Inductively Coupled Plasma Optical Emission Spectroscopy.** The solubility of LiAl-LDH in 3 M LiOH in $D_2O$ at room temperature was acquired by dispersing gibbsite (500 mM) in 3 M LiOH in $D_2O$ in a glovebox. Nine dispersions were equilibrated for approximately one month. Each dispersion was centrifuged, and the supernatant was acidified with nitric acid (GFS Chemicals, Inc. Cat. 621). The samples were analyzed for $Al^{3+}$ using a PerkinElmer Optima 8300 dual view inductively coupled plasma-optical emission spectrometer (ICP-OES) and a PerkinElmer S-10 autosampler interface.

## 3. RESULTS AND DISCUSSION

While the transformation of gibbsite into LiAl-LDH via dispersion in 3 M LiOH proceeds spontaneously at ambient temperature, comparable studies dispersing gibbsite in 3 M LiCl or 3 M $LiNO_3$ in $D_2O$ led to no XRD apparent $Li[Al(OH)_3)]_2Cl{\cdot}nH_2O$ or $Li[Al(OH)_3)]_2NO_3{\cdot}nH_2O$ phases, respectively (Figure S4). Thus, the formation of LiAl-LDH at room temperature, either by solid-state intercalation or dissolution/reprecipitation pathways, likely requires caustic hydroxide solutions.

To determine the equilibrium solubility of LiAl-LDH, gibbsite was allowed to react with 3 M LiOH in $D_2O$ for ca. 1 month at room temperature. After this time, an $Al^{3+}$ concentration of 10 mM was measured in solution by ICP-OES. For comparison, the equilibrium solubility of gibbsite in 3 M NaOH is approximately 200 mM at room temperature.[41]

*In situ* $^{27}Al$ MAS NMR studies were conducted to develop a quantitative understanding of the transient aluminate ion ($Al(OH)_4^-$) concentration in solution and how this influences the evolution of solid phases (Figure 2). Both solution $T_d$ $Al^{3+}$ species (i.e., aluminate ions) and solid $O_h$ $Al^{3+}$ species (i.e., gibbsite and LiAl-LDH) could be observed with this technique, as they exhibited vastly different chemical shifts (approximately 80 ppm vs 10 ppm for solution and solid species, respectively). Selective excitation pulse widths were used to acquire the *in situ* $^{27}Al$ spectra at 7.0 T to suppress the broad $O_h$ spinning



DOI: 10.1021/acs.inorgchem.9b02000
Inorg. Chem. 2019, 58, 12385−12394

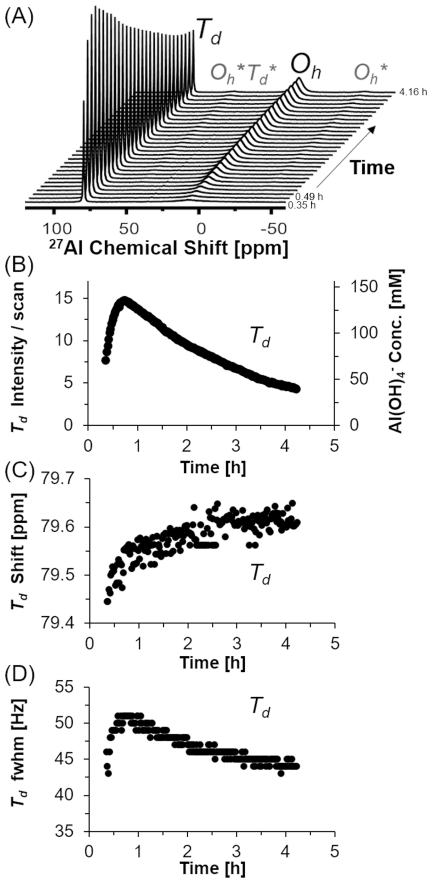


**Figure 2.** (A) $^{27}$Al MAS NMR spectra during the isothermal reaction of 0.5 M gibbsite in deuterated 3 M LiOH. The spinning side bands are denoted * and attributed to either the $T_d$ or $O_h$ resonance. Every seventh spectrum is shown. (B) Variation in the integrated NMR signal intensity of the $T_d$ resonance and the experimental concentration of aluminate ($Al(OH)_4^-$) ions as a function of time, see Supporting Information for additional details. (C) Time-resolved $^{27}$Al NMR $T_d$ chemical shift and (D) $T_d$ full width half-maximum (fwhm) estimated by Lorentzian/Gaussian line shapes.

sidebands arising from gibbsite which overlap with the $T_d$ aluminate resonance and to reduce the transients needed for spectra detailing the aluminate ion concentration profile.

Determining the concentration profile of metastable $Al^{3+}$ $T_d$ species (aluminate ions, Figure 2B) during the transformation of gibbsite to LiAl-LDH is nontrivial and was achieved using external references (Figure S5, 2 mM $Al(OH)_4^-$ in deuterated 3 M LiOH, 2 mM $Al(OH)_4^-$ in deuterated 3 M NaOH, and 100 mM $Al(OH)_4^-$ in deuterated 3 M NaOH). Spectra acquired during the *in situ* experiment indicate that the concentration of aluminate ions in solution increases rapidly to a maximum of over 100 mM by ca. 1 h of reaction, which can be attributed to the dissolution of gibbsite (eq 1). Despite the rather large supersaturation with respect to LiAl-LDH, the concentration of aluminate ions in solution initially appears to be driven solely by equilibration with gibbsite (eq 1). The decrease in concentration after ca. 1 h is consistent with the eventual emergence of LiAl-LDH as the solubility-limiting phase.

After 4 h of reaction, the $T_d$ chemical shift increased from ca. 79.5 to 79.6 ppm (Figure 2C). Notably, the initial ($t$ < 1 h) positive correlation between the chemical shift and full width half-maximum (fwhm) of the $T_d$ signal fraction is consistent with prior observations of aluminate in NaOH systems, although the magnitude of the change in the chemical shift position greatly exceeded that observed in the NaOH system[41] (e.g., 0.02 ppm in 3 M NaOH vs 0.1 ppm in 3 M LiOH). While the temperature was controlled at 25 °C during the *in situ* run, we also explored the sensitivity of the $^{27}$Al shift to temperature variation by collecting $^{27}$Al-MAS NMR spectra of 2 mM $Al(OH)_4^-$ in 3 M LiOH in $D_2O$ between the temperatures of 25 and 100 °C. The spectra (Figure S6) demonstrate that the observed variation in $^{27}$Al chemical shift far exceeds those which would arise from inadvertent sample heating, and heating reduces the $T_d$ resonance's fwhm, which is in contrast with the observed, *in situ* $^{27}$Al MAS NMR results observed at $t$ < 1 h in Figure 2D.

We instead attribute the trend in chemical shift to strong shielding of the $Al^{3+}$ nucleus that is dependent on LiOH concentration,[28] thus a decrease in [$Li^+$] and [$OH^-$] in the solution upon precipitation is consistent with the observed deshielding. The deshielding of the $T_d$ resonance in the LiOH system during the course of the reaction may relate to (i) the decrease in solution concentrations of $Li^+$ and $OH^-$ following formation of LiAl-LDH and/or (ii) an evolving ensemble of $Li^+\cdots Al(OH)_4^-$ ion−ion distances as aluminate concentrations change over time. The $Li^+\cdots Al(OH)_4^-$ ion distance may be particularly important to the formation of LiAl-LDH because ion-pairing distorts the $Al(OH)_4^-$ tetrahedron.[42] Ion pairing between $Li^+$ and $OH^-$ results in an increased delocalization of protons in water molecules solvating the ion pair.[43] The delocalization is attenuated in deuterated solutions.[43] However, relating this ensemble of ion−ion distances and their corresponding solvation shells to the rapid precipitation kinetics in LiOH solutions compared to NaOH and KOH solutions remains an active area of research.

While the position of the $T_d$ signal exhibits a continuous downfield trend, the trend in $T_d$ fwhm is more complex (Figure 2D). The $T_d$ fwhm initially increased from 43 to 51 Hz and then decreased to 44 Hz at $t$ = 1.1 h. The initial 2 Hz increase in fwhm at $t$ < 1 h may have been due to an increase in viscosity of the system as a result of the increase in aluminate ions in solution. The reduction in fwhm during later stages of intercalation (1 h < $t$) is consistent with the reduction of aluminate ion concentrations and, to a much lesser extent, reduction in $Li^+$ and $OH^-$ concentrations in solution, all of which reduce the viscosity of the solution and the fwhm of the $^{27}$Al resonance.[28,44]

The region of the spectrum showing the $O_h$ resonance during the *in situ* $^{27}$Al MAS NMR study of gibbsite in 3 M LiOH (Figure 2A) is shown in Figure 3A. Importantly, the low field strength (7.0 T) and slow spinning rate (ca. 3 kHz) are insufficient to resolve aluminum sites with large quadrupole coupling parameters.[45]

Qualitatively, while there is some scatter in the $O_h$ chemical shift (Figure 3B), the overall trend is that the resonance becomes shielded as the reaction proceeds. The as-synthesized gibbsite dispersed in LiOH (3 M) exhibits an $O_h$ $^{27}$Al fwhm greater than 1500 Hz resonating at approximately 10 ppm (Figure 3C). During gibbsite dissolution and formation of LiAl-LDH, the central band $O_h$ resonance progressively narrows over a few hours to about 400 Hz, as estimated with a mixed Lorentzian−Gaussian line shape. This reduction in fwhm is likely due to the smaller $^{27}$Al quadrupolar coupling constant ($C_Q$) for LiAl-LDH compared to the initial gibbsite (4.7 and 2.2 MHz for the gibbsite sites[32] and 1.7 MHz for


DOI: 10.1021/acs.inorgchem.9b02000
*Inorg. Chem.* 2019, 58, 12385−12394

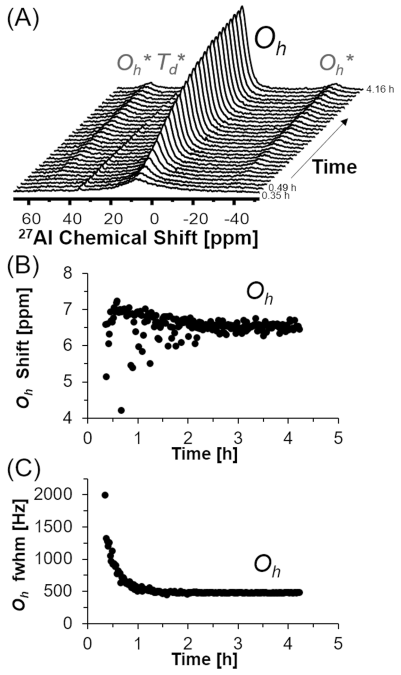


**Figure 3.** (A) $^{27}$Al MAS NMR spectra of the $O_h$ region during the isothermal intercalation of 0.5 M gibbsite in 3 M LiOH in $D_2O$. The spectra are equivalent to Figure 2A but vertically magnified by a factor of 6. Every seventh spectrum is shown. The $O_h$ $^{27}$Al resonance's (B) chemical shift and (C) fwhm as estimated with a mixed Lorentzian–Gaussian line shape.

LiAl-LDH (Table S1)). At intermediate reaction times, the local disorder arising from $Al^{3+}$ in partially lithiated hydroxide sheets may attenuate this narrowing.[46]

The field strength (7.0 T) and spinning rate (3 kHz) of the *in situ* study results in better detection of LiAl-LDH than the initial gibbsite, as is evident by the overall increase in signal in the $O_h$ region during the reaction. The central band fwhm and intensity strongly correlates with fwhm and intensity of the spinning side bands (SSB, $O_h$* in Figure 3A). Previous literature suggests that the broadening of the SSB in LDH is not only attributed to a disorder-based distribution of chemical shifts and quadrupolar interactions but is also influenced by changes in the hydration sphere of the intercalated anion, if the SSB changes independently of the $O_h$ $^{27}$Al MAS NMR central transition.[47] Given the strong correlation with the $O_h$ $^{27}$Al central transition intensity and fwhm, the emergence of relatively sharp SSB is consistent with the relatively low $C_Q$ of LiAl-LDH, likely broadened by local disorder in the hydroxide sheet at intermediate times.[32,46]

Gibbsite and LiAl LDH are poorly resolved at this field strength and spinning rate.[45] To quantify the relative amounts of gibbsite and LiAl-LDH, we conducted XRD and *ex situ* $^{27}$Al studies at a field strength of 20.0 T.

XRD patterns of the solid phase as a function of reaction time are shown in Figure 4. The XRD pattern of the product, LiAl-LDH, contains asymmetric diffraction peaks in the region between $2\theta$ = 19.5 and 26° attributed to disordered stacking of $LiAl_2(OH)_6^+$ layers, where small shifts of $Li^+$ positions averaged over many layers produce a pseudohexagonal unit cell that also contains anisotropic strain.[20] More recent work on similar aluminum layered double hydroxides (albeit with $Cl^-$ and not $OH^-$ intercalation) explored the asymmetry between adjacent metal hydroxide sheets and polytypism of these materials.[48] In this work, intermediate compositions were determined using a Pawley refinement with a hexagonal cell for LiAl-LDH. The XRD patterns were analyzed both with and without the inclusion of preferential orientation, with typical refinements shown in Figures S7–S9.

As the reaction proceeds, the prevalence and crystal domain size of gibbsite decrease monotonically, and after 2 h, the gibbsite phase is below the limit of detection via XRD. We note that the limit of detection of gibbsite in mixtures of LiAl-LDH is approximately 3 wt % with the utilized XRD diffractometer as shown in Figure S10. Including preferential orientation in the Pawley refinement negligibly affected the acquired phase composition and crystal domain size of

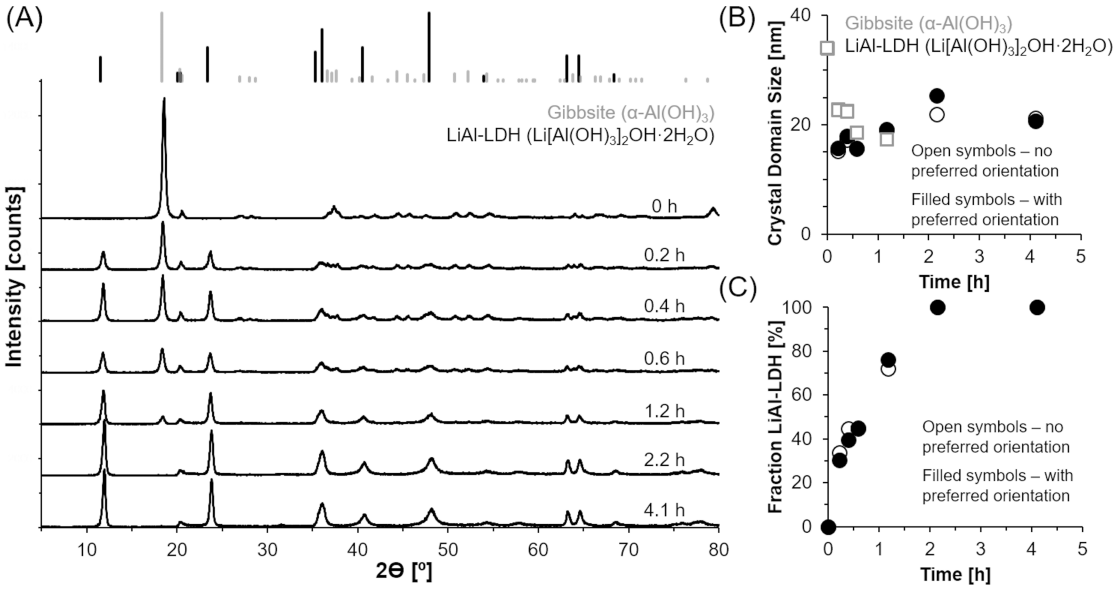


**Figure 4.** (A) Time series of powder X-ray diffraction patterns during the dispersion of 0.5 M gibbsite in 3 M LiOH. (B) Crystal domain sizes of LiAl-LDH ($Li[Al(OH)_3]_2OH{\cdot}2H_2O$) and gibbsite. (C) The fraction of LiAl-LDH in the mixture as calculated via a Pawley refinement in TOPAS. Example XRD fits are shown in Figures S7–S9.



DOI: 10.1021/acs.inorgchem.9b02000
*Inorg. Chem.* 2019, 58, 12385–12394

gibbsite. The crystal domain size of LiAl-LDH increases insignificantly from ca. 18 to 20 nm as the reaction proceeds, with limited influence of preferential orientation on refinement results. In this system, concurrent dissolution of gibbsite and precipitation of LiAl-LDH likely results in an ensemble of crystal domain sizes, in which the distribution's average becomes marginally larger. Importantly, the XRD patterns provide evidence that residual gibbsite remains throughout the first 1.2 h of the reaction. This residual gibbsite is likely the solubility-limiting phase, with respect to the aluminate ion concentration, during the *in situ* $^{27}$Al MAS NMR experiments at 7.0 T. To better resolve changes in the solid phase, $^{6}$Li and $^{27}$Al MAS NMR were conducted at a higher field strength (20.0 T).

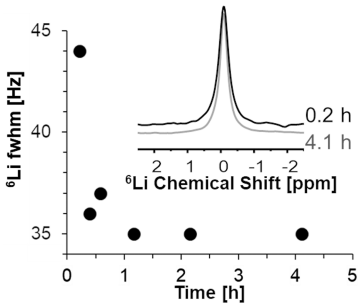


**Figure 5.** $^{6}$Li fwhm is determined via Gaussian fitting. (Inset) High field, 20.0 T, $^{6}$Li MAS NMR spectra (spectra are offset and normalized to the same vertical height). Additional $^{6}$Li MAS NMR spectra are shown in Figure S11.

$^{6}$Li MAS NMR spectra at 20.0 T are shown in Figure 5. The $^{6}$Li resonance occurs at approximately $\delta = -0.08$ ppm (relative to 1 M LiCl in water) and lacks spinning side bands (Figure S11). Prior $^{6}$Li MAS NMR studies demonstrate that the chemical shifts for $Li^+$ in $O_h$ coordination in lithium aluminates vary between 0.31 and −0.4 ppm in $LiAl_5O_8$ and $\alpha$-$LiAlO_2$, respectively, with a comparable chemical shift of −0.05 ppm for $Li_2Al(OH)_6Cl{\cdot}nH_2O$.[49] The $^{6}$Li chemical shift found in this study ($\delta = -0.08$ ppm) did not vary significantly during the course of the topotactic transformation of gibbsite into LiAl-LDH, but a subtle reduction of the $^{6}$Li fwhm occurs. The decrease from 44 to 35 Hz fwhm was estimated by fitting Gaussian line shapes (shown in Figure S11). This fwhm reduction is attributed to an increase in the local-range order of the metal hydroxide sheet (Figure 1) after filling $Li^+$ vacancies in the hydroxide sheet predominantly present at early stages of the reaction. However, in addition to the increase in local order, the reduction in fwhm may also be attributed to an increase in $Li^+$ ion mobility. The mobility of $Li^+$ ions[50−53] implies that $OH^-$ ions are simultaneously mobile, as was found in $OH^-$ based LDH electrolytes[54] and molecular dynamics simulations of jump diffusion in LDH materials.[55] All spectra are well fit by a single Gaussian line shape with no evidence of a superimposed broad signal.[3] The superimposed broad resonance was previously attributed to $Li^+$ in an amorphous solid found after dispersing gibbsite in very concentrated LiCl solutions.[3]

$^{27}$Al MAS NMR spectra at 20.0 T of the solid phases are shown in Figure 6. In the $O_h$ $Al^{3+}$ coordination region of the spectra, gibbsite and LiAl-LDH can be partially resolved,

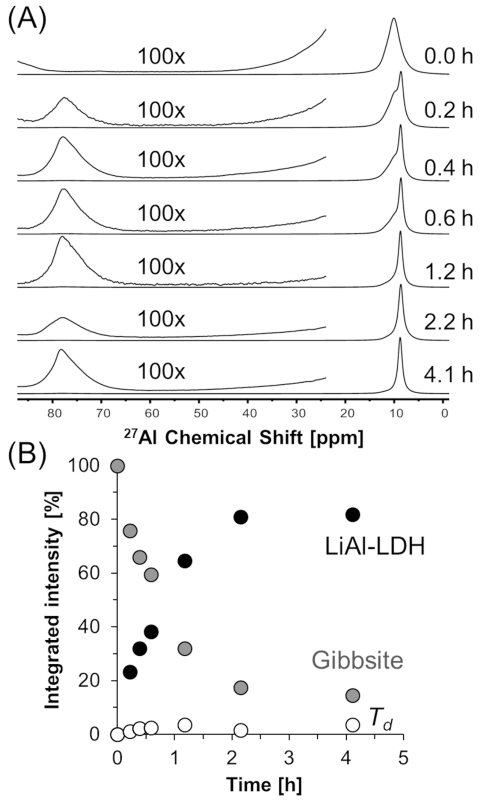


**Figure 6.** (A) High field (20.0 T) $^{27}$Al MAS NMR spectra. The spectrum at 0 h, corresponding with the initial spectrum of gibbsite, was published previously.[57] (B) Summary of the deconvoluted $^{27}$Al MAS NMR resonances. The quadrupolar coupling parameters are listed and the fits are shown in Table S1 and Figures S13−S15, respectively. Resonances of $O_h$ $Al^{3+}$ sites near defects, such as $Li^+$ vacancies, may overlap with those of the original gibbsite.

consistent with recent studies of LDH materials at comparable field strengths.[32,46,56] During the course of the reaction, a narrow $O_h$ Al peak ($C_Q$ < 1.7 MHz) emerges upfield of the initial $^{27}$Al resonances of gibbsite.[57] This emergent peak is well resolved in complementary $^{27}$Al MQMAS spectra (Figure S12). Deconvolution of the signal intensity of LiAl-LDH (Figures S13−S15) was performed in DMFIT, using fixed quadrupolar coupling parameters for the two octahedral gibbsite sites (site 1: $\delta_{iso}$ = 10.75 ppm, $C_Q$ = 2.2 MHz, and $\eta_Q$ = 0.7; site 2: $\delta_{iso}$ = 12.97 ppm, $C_Q$ = 4.7 MHz, and $\eta_Q$ = 0.4),[40,58] and regressed the single Al site quadrupolar coupling parameters corresponding to the LiAl-LDH phase. These parameters are listed in Table S1, and the corresponding fits to the data are included.

In accordance with prior studies,[56] spectra were fit with the lowest number of peaks (3) required to achieve a satisfactory fit. With the exception of the initial gibbsite, this resulted in an unequal site distribution in the two gibbsite Al sites, which suggests the presence of additional Al sites indistinguishable at a field strength of 20.0 T in extreme overlap with the gibbsite resonances. While this asymmetric broadening is attributed to gibbsite in Figure 6B, there is no XRD apparent gibbsite in Figure 4 at 2.2 or 4.1 h. Similar asymmetry in the $O_h$ resonance in ca. 20.0 T $^{27}$Al MAS NMR spectra of zinc or magnesium aluminum layered double hydroxides was attributed to local disorder comprising structural defects and vacancies in the metal hydroxide sheet,[46,59] which manifest in an $Al^{3+}$ site heterogeneity and a distribution of quadrupolar coupling


DOI: 10.1021/acs.inorgchem.9b02000
*Inorg. Chem.* 2019, 58, 12385−12394

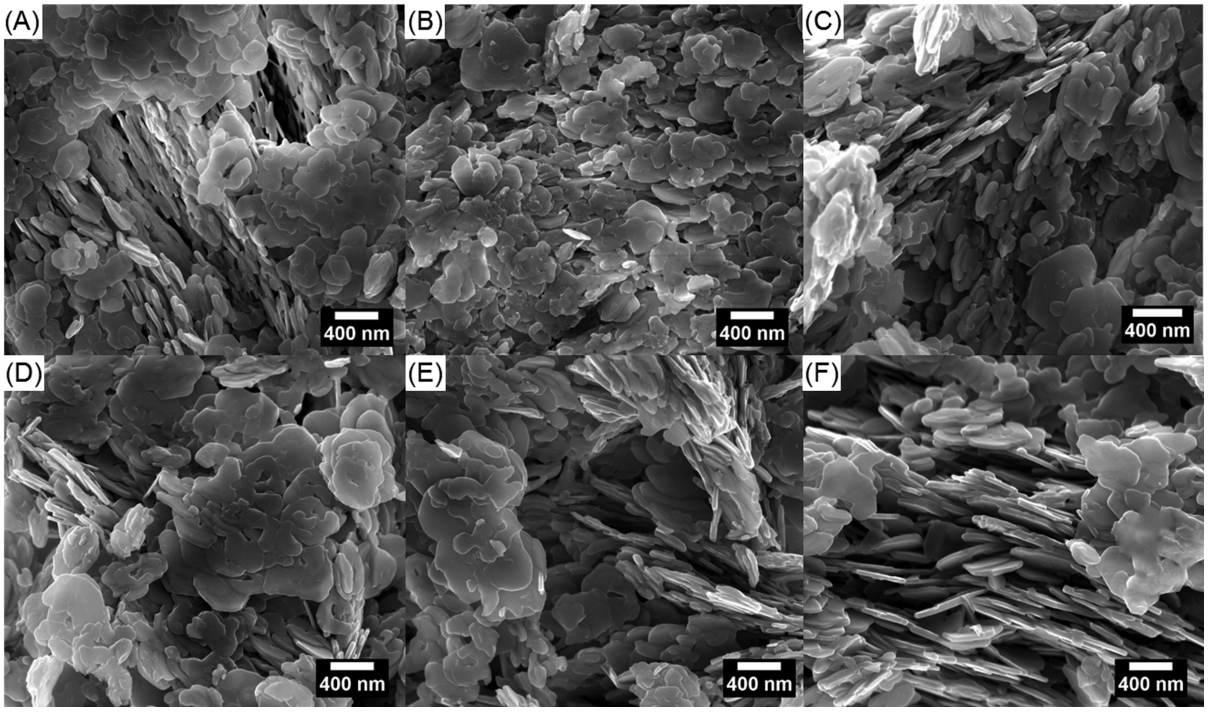


**Figure 7.** Scanning electron microscopy of the harvested solids tracking 0.5 M gibbsite dispersed in 3 M LiOH in $D_2O$. The solids after (A) 0.2 h, (B) 0.4 h, (C) 0.6 h, (D) 1.2 h, (E) 2.2 h, and (F) 4.1 h are shown. An SEM micrograph of as-synthesized gibbsite is shown in Figure S16.

constants. It is possible that resonances of $Al^{3+}$ $O_h$ sites proximal to defects and vacancies overlap with those of the original gibbsite. The relative integral of the two sites attributed to gibbsite, the LiAl-LDH site, and the $T_d$ sites are shown in Figure 6B. The final spectra after the 4.1 h reaction are dominated by a narrow resonance ($C_Q$ = ca. 1.6 MHz, $\eta_Q$ = ca. 0) but still exhibit asymmetric broadening downfield (ca. 15% of the total signal), which is well fit by resonances assigned to gibbsite, albeit with disproportionate site intensities.

The generation of under-coordinated $Al^{3+}$ species was also investigated with high field $^{27}Al$ NMR. Previous $^{27}Al$ NMR measurements demonstrated that gibbsite crystallized from an amorphous $Al(OH)_3$ gel contains minor fractions of tetrahedral ($T_d$; <1% total signal) and penta-coordinate $Al^{3+}$ ($Al_P$; <2% total signal), likely associated with the surface,[60] that increase in prevalence following dehydration.[57,60] In this study, the signal intensity of the $T_d$ resonances associated with the solid phase varies between 1 and 4%, far exceeding that of the initial gibbsite. The increased prevalence of the $T_d$ species throughout the course of the reaction compared to the starting gibbsite may arise from (i) sorption of solution state aluminate ions and/or (ii) generation of undercoordinated $Al^{3+}$ species at the exterior surface, or at defect-rich,[61] subsurface lithiated-delithiated boundaries, such as an interface between gibbsite and LiAl-LDH. In a computational study, $Al_P$ sites were suggested to be short-lived intermediates in gibbsite dissolution and precipitation processes.[62] However, there are negligible quantities (<0.1%) of $Al_P$ sites associated with the solid phase in this system (Figure 6A).[60] The fraction of trace $T_d$ $Al^{3+}$ was previously correlated to nanoparticle size,[60] therefore SEM was conducted to evaluate whether the increased prevalence of $T_d$ Al corresponded with a drastic reduction in primary particle size.

SEM images of the solids harvested during the reaction of gibbsite in deuterated LiOH are shown in Figure 7. The coarsening of edges of euhedral nanoplates after reaction is consistent with the dissolution of gibbsite. At intermediate time points during the reaction, a fraction of smaller nanoparticles is also formed, likely due to the reprecipitation of aluminate ions that are produced from $OH^-$-mediated dissolution of gibbsite. A comparison of the initial gibbsite and the $Li[Al(OH)_3]_2OH{\cdot}2H_2O$ produced after 4.1 h of reaction shows that the majority of particles retained the approximate size and plate-like morphology of the starting material (Figure S16). However, the exact extent of homogeneous and surface mediated precipitation of aluminate ions in this transformation remains unclear. In this regard, the emergence of metastable aluminate ions in solution and elevated $T_d$ aluminum sites in the harvested solids at intermediate reaction times point to rather complicated interfacial dynamics, involving multiple dissolution, precipitation, and intercalation steps, which clearly deviate from the simple assumptions used in classical lithium intercalation models.[63]

## 4. CONCLUSIONS

*In situ* MAS NMR and multimethod characterization enabled new insights into pathways controlling the transformation of gibbsite to LiAl-LDH in LiOH. In particular, relevant to the often invoked solid-state intercalation pathway, the importance, if not dominance, of the dissolution-reprecipitation pathway in caustic solution is now evident. The concentration of aluminate ions in solution shows a shift of solubility control from the dissolution of gibbsite at early reaction stages to the emergence of much less soluble LiAl-LDH. After this shift, free aluminate ions become increasingly subsumed into LiAl-LDH precipitation. Despite the narrowing of SSB and the central $O_h$ transition at 7.0 T, the crystal domain size of LiAl-LDH, as determined by XRD, only marginally increases during the



DOI: 10.1021/acs.inorgchem.9b02000
*Inorg. Chem.* 2019, 58, 12385−12394

process. *Ex situ* $^{27}$Al MAS NMR spectra at 20.0 T reveal both the increase in $T_d$ $Al^{3+}$ sites in reacted solids and the residual asymmetry in the $O_h$ central transition at longer reaction times, despite no remaining gibbsite detectable by XRD.

This study highlights the unique capabilities of (i) *in situ* MAS NMR to provide insight into the aluminate ion solution concentration and the influence this has on LDH formation mechanisms in caustic solutions and (ii) *ex situ* MAS NMR to detect the local ordering in LADH before the emergence of long-range crystalline order detectable by XRD.

Furthermore, the improved understanding of this transformation mechanism hints at the potential to tune the structure and reactivity of LDHs in this system for specific applications through manipulation of reaction conditions. This mechanistic understanding may enable the deployment of LiOH to control the concentration of $Al^{3+}$ in caustic solutions of high level nuclear waste and improve waste processing efficiency.

## ■ ASSOCIATED CONTENT

### Supporting Information

The Supporting Information is available free of charge on the ACS Publications website at DOI: 10.1021/acs.inorgchem.9b02000.

$^{27}$Al MAS NMR, XRD, $^{6}$Li MAS NMR, and SEM results and analyses (PDF)

## ■ AUTHOR INFORMATION


### Corresponding Authors

*E-mail: trenton.graham@pnnl.gov.
*E-mail: Carolyn.pearce@pnnl.gov.

### ORCID

Trent R. Graham: 0000-0001-8907-8004
Jian Zhi Hu: 0000-0001-8879-747X
Xin Zhang: 0000-0003-2000-858X
Mateusz Dembowski: 0000-0002-6665-8417
Nicholas R. Jaegers: 0000-0002-9930-7672
Kevin M. Rosso: 0000-0002-8474-7720
Carolyn I. Pearce: 0000-0003-3098-1615


### Notes

The authors declare no competing financial interest.

## ■ ACKNOWLEDGMENTS

This research was supported by IDREAM (Interfacial Dynamics in Radioactive Environments and Materials), an Energy Frontier Research Center funded by the U.S. Department of Energy (DOE), Office of Science, Basic Energy Sciences (BES). Characterization was performed using facilities at the Environmental Molecular Science Laboratory (EMSL, grid.436923.9), a DOE Office of Science User Facility sponsored by the Office of Biological and Environmental Research at Pacific Northwest National Laboratory (PNNL). PNNL is a multiprogram national laboratory operated for DOE by Battelle Memorial Institute operating under Contract No. DE-AC05-76RL0-1830. T.R.G. is grateful for support from the PNNL - Washington State University (WSU) Distinguished Graduate Research Program. The authors acknowledge Ian Leavy and Steven Baum for ICP-OES measurements.

## ■ REFERENCES


(1) Li, L.; Deshmane, V. G.; Paranthaman, M. P.; Bhave, R.; Moyer, B. A.; Harrison, S. Lithium Recovery from Aqueous Resources and Batteries: A Brief Review. *Johnson Matthey Technol. Rev.* **2018**, *62*, 161−176.

(2) Paranthaman, M. P.; Li, L.; Luo, J.; Hoke, T.; Ucar, H.; Moyer, B. A.; Harrison, S. Recovery of Lithium from Geothermal Brine with Lithium-Aluminum Layered Double Hydroxide Chloride Sorbents. *Environ. Sci. Technol.* **2017**, *51*, 13481−13486.

(3) Wimpenny, J.; Colla, C. A.; Yu, P.; Yin, Q. Z.; Rustad, J. R.; Casey, W. H. Lithium Isotope Fractionation during Uptake by Gibbsite. *Geochim. Cosmochim. Acta* **2015**, *168*, 133−150.

(4) Fogg, A. M.; Dunn, J. S.; Shyu, S. G.; Cary, D. R.; O'Hare, D. Selective Ion-Exchange Intercalation of Isomeric Dicarboxylate Anions into the Layered Double Hydroxide $[LiAl_2(OH)_6]Cl{\bullet}H_2O$. *Chem. Mater.* **1998**, *10*, 351−355.

(5) Kaassis, A. Y. A.; Xu, S. M.; Guan, S.; Evans, D. G.; Wei, M.; Williams, G. R. Hydroxy Double Salts Loaded with Bioactive Ions: Synthesis, Intercalation Mechanisms, and Functional Performance. *J. Solid State Chem.* **2016**, *238*, 129−138.

(6) Lin, K.; Luo, X.; Pan, X.; Zhang, C.; Liu, Y. Enhanced Corrosion Resistance of LiAl- Layered Double Hydroxide (LDH) Coating Modified with a Schiff Base Salt on Aluminum Alloy by One Step In-Situ Synthesis at Low Temperature. *Appl. Surf. Sci.* **2019**, *463*, 1085−1096.

(7) Zheludkevich, M. L.; Poznyak, S. K.; Rodrigues, L. M.; Raps, D.; Hack, T.; Dick, L. F.; Nunes, T.; Ferreira, M. G. S. Active Protection Coatings with Layered Double Hydroxide Nanocontainers of Corrosion Inhibitor. *Corros. Sci.* **2010**, *52*, 602−611.

(8) Gharbi, O.; Thomas, S.; Smith, C.; Birbilis, N. Chromate Replacement: What Does the Future Hold? *npj Mater. Degrad.* **2018**, *2*, 1−8.

(9) Huang, L.; Wang, J.; Gao, Y.; Qiao, Y.; Zheng, Q.; Guo, Z.; Zhao, Y.; O'Hare, D.; Wang, Q. Synthesis of $LiAl_2$-Layered Double Hydroxides for $CO_2$ Capture over a Wide Temperature Range. *J. Mater. Chem. A* **2014**, *2*, 18454−18462.

(10) Hosni, K.; Abdelkarim, O.; Frini-Srasra, N.; Srasra, E. Synthesis, Structure and Photocatalytic Activity of Calcined Mg-Al-Ti-Layered Double Hydroxides. *Korean J. Chem. Eng.* **2015**, *32*, 104−112.

(11) Zhao, Y.; Jia, X.; Waterhouse, G. I. N.; Wu, L.-Z.; Tung, C.-H.; O'Hare, D.; Zhang, T. Layered Double Hydroxide Nanostructured Photocatalysts for Renewable Energy Production. *Adv. Energy Mater.* **2016**, *6*, 1501974.

(12) Li, P.; Yu, F.; Altaf, N.; Zhu, M.; Li, J.; Dai, B.; Wang, Q. Two-Dimensional Layered Double Hydroxides for Reactions of Methanation and Methane Reforming in C1 Chemistry. *Materials* **2018**, *11*, 221.

(13) Williams, G. R.; Moorhouse, S. J.; Prior, T. J.; Fogg, A. M.; Rees, N. H.; O'Hare, D. New Insights into the Intercalation Chemistry of $Al(OH)_3$. *Dalt. Trans.* **2011**, *40*, 6012−6022.

(14) Britto, S.; Kamath, P. V. Structure of Bayerite-Based Lithium−Aluminum Layered Double Hydroxides (LDHs): Observation of Monoclinic Symmetry. *Inorg. Chem.* **2009**, *48*, 11646−11654.

(15) Khan, A. I.; O'Hare, D. Intercalation Chemistry of Layered Double Hydroxides: Recent Developments and Applications. *J. Mater. Chem.* **2002**, *12*, 3191−3198.

(16) Zhao, Y.; Hu, H.; Yang, X.; Yan, D.; Dai, Q. Tunable Electronic Transport Properties of 2D Layered Double Hydroxide Crystalline Microsheets with Varied Chemical Compositions. *Small* **2016**, *12*, 4471−4476.

(17) Shin, J.; Choi, C. J.; Kim, T. H.; Oh, J. M. Phase Transformation from Brucite to Highly Crystalline Layered Double Hydroxide through a Combined Dissolution-Reprecipitation and Substitution Mechanism. *Cryst. Growth Des.* **2018**, *18*, 5398−5405.

(18) Besserguenev, A. V.; Fogg, A. M.; Francis, R. J.; Price, S. J.; O'Hare, D.; Isupov, V. P.; Tolochko, B. P. Synthesis and Structure of the Gibbsite Intercalation Compounds $[LiAl_2(OH)_6]X$ {X = Cl, Br, $NO_3$} and $[LiAl_2(OH)_6]Cl{\cdot}H_2O$ Using Synchrotron X-Ray and Neutron Powder Diffraction. *Chem. Mater.* **1997**, *9*, 241−247.




DOI: 10.1021/acs.inorgchem.9b02000
*Inorg. Chem.* 2019, 58, 12385−12394

(19) Poeppelmeier, K. R.; Hwu, S. J. Synthesis of Lithium Dialuminate by Salt Imbibition. *Inorg. Chem.* **1987**, *26*, 3297−3302.
(20) Thiel, J.; Chiang, C.; Poeppelmeier, K. Structure of Lithium Aluminum Hydroxide Dihydrate ($LiAl_2(OH)_7•2H_2O$). *Chem. Mater.* **1993**, *5*, 297−304.
(21) Paudel, H. P.; Lee, Y. L.; Senor, D. J.; Duan, Y. Tritium Diffusion Pathways in $\gamma$-$LiAlO_2$ Pellets Used in TPBAR: A First-Principles Density Functional Theory Investigation. *J. Phys. Chem. C* **2018**, *122*, 9755−9765.
(22) Witt, E.; Nakhal, S.; Chandran, C. V.; Lerch, M.; Heitjans, P. NMR and Impedance Spectroscopy Studies on Lithium Ion Diffusion in Microcrystalline $\gamma$-LiAlO2. *Z. Phys. Chem.* **2015**, *229*, 1327−1339.
(23) Antolini, E. The Stability of $LiAlO_2$ Powders and Electrolyte Matrices in Molten Carbonate Fuel Cell Environment. *Ceram. Int.* **2013**, *39*, 3463−3478.
(24) Fang, Z.-K.; Zhu, Y.-R.; Yi, T.-F.; Xie, Y. $Li_4Ti_5O_{12}$−$LiAlO_2$ Composite as High Performance Anode Material for Lithium-Ion Battery. *ACS Sustainable Chem. Eng.* **2016**, *4*, 1994−2003.
(25) Sams, T. L.; Guillot, S. *Aluminum Removal and Sodium Hydroxide Regeneration from Hanford Tank Waste by Lithium Hydrotalcite Precipitation: Summary of Prior Lab-Scale Testing* **2011**, DOI: 10.2172/1010331.
(26) Sams, T. L.; Massie, H. L. *Aluminum Readiness Evaluation For Aluminum Removal and Sodium Hydroxide Regeneration From Hanford Tank Waste By Lithium Hydrotalcite Precipitation* **2011**, DOI: 10.2172/1010336.
(27) Reynolds, J. G.; McCoskey, J. K.; Herting, D. L. Gibbsite Solubility in Hanford Nuclear Waste Approached from above and below Saturation. *Ind. Eng. Chem. Res.* **2016**, *55*, 5465−5473.
(28) Sipos, P. The Structure of Al(III) in Strongly Alkaline Aluminate Solutions − A Review. *J. Mol. Liq.* **2009**, *146*, 1−14.
(29) Van Straten, H. A.; Schoonen, M. A. A.; De Bruyn, P. L. Precipitation from Supersaturated Aluminate Solutions. III. Influence of Alkali Ions with Special Reference to $Li^+$. *J. Colloid Interface Sci.* **1985**, *103*, 493−507.
(30) Frenzel, J.; Oliveira, A. F.; Duarte, H. A.; Heine, T.; Seifert, G. Structural and Electronic Properties of Bulk Gibbsite and Gibbsite Surfaces. *Z. Anorg. Allg. Chem.* **2005**, *631*, 1267−1271.
(31) Isupov, V. P.; Gabuda, S. P.; Kozlova, S. G.; Chupakhina, L. É. Structural Mechanism of Selective Binding of Lithium on a Solid Matrix of $Al(OH)_3$ from Aqueous Solutions. *J. Struct. Chem.* **1998**, *39*, 362−366.
(32) Kozlova, S. G.; Gabuda, S. P.; Isupov, V. P.; Chupakhina, L. É. Using NMR in Structural Studies of Aluminum Hydroxide Intercalation Compounds with Lithium Salts. *J. Struct. Chem.* **2003**, *44*, 198−205.
(33) Balan, E.; Lazzeri, M.; Morin, G.; Mauri, F. First-Principles Study of the OH-Stretching Modes of Gibbsite. *Am. Mineral.* **2006**, *91*, 115−119.
(34) Kim, D.; Jung, J.; Ihm, J. Theoretical Study of Aluminum Hydroxide as a Hydrogen- Bonded Layered Material. *Nanomaterials* **2018**, *8*, 375.
(35) Fogg, A. M.; O'Hare, D. Study of the Intercalation of Lithium Salt in Gibbsite Using Time- Resolved in situ X-Ray Diffraction. *Chem. Mater.* **1999**, *11*, 1771−1775.
(36) Williams, G. R.; O'Hare, D. A Kinetic Study of the Intercalation of Lithium Salts into $Al(OH)_3$. *J. Phys. Chem. B* **2006**, *110*, 10619−10629.
(37) Hu, J. Z.; Hu, M. Y.; Zhao, Z.; Xu, S.; Vjunov, A.; Shi, H.; Camaioni, D. M.; Peden, C. H. F.; Lercher, J. A. Sealed Rotors for in Situ High Temperature High Pressure MAS NMR. *Chem. Commun.* **2015**, *51*, 13458−13461.
(38) Zhang, X.; Zhang, X.; Graham, T. R.; Pearce, C. I.; Mehdi, B. L.; N'Diaye, A. T.; Kerisit, S.; Browning, N. D.; Clark, S. B.; Rosso, K. M. Fast Synthesis of Gibbsite Nanoplates and Process Optimization Using Box-Behnken Experimental Design. *Cryst. Growth Des.* **2017**, *17*, 6801−6808.
(39) Raiford, D. S.; Fisk, C. L.; Becker, E. D. Calibration of Methanol and Ethylene Glycol Nuclear Magnetic Resonance Thermometers. *Anal. Chem.* **1979**, *51*, 2050−2051.
(40) Chandran, C.; Kirschhock, C. E. A.; Radhakrishnan, S.; Taulelle, F.; Martens, J. A.; Breynaert, E. Alumina: Discriminative Analysis Using 3D Correlation of Solid-State NMR Parameters. *Chem. Soc. Rev.* **2019**, *48*, 134−156.
(41) Graham, T. R.; Dembowski, M.; Martinez-Baez, E.; Zhang, X.; Jaegers, N. R.; Hu, J.; Gruszkiewicz, M. S.; Wang, H.-W.; Stack, A. G.; Bowden, M. E.; Delegard, C. H.; Schenter, G. K.; Clark, A. E.; Clark, S. B.; Felmy, A. R.; Rosso, K. M.; Pearce, C. I.; et al. In Situ $^{27}$Al NMR Spectroscopy of Aluminate in Sodium Hydroxide Solutions above and below Saturation with Respect to Gibbsite. *Inorg. Chem.* **2018**, *57*, 11864−11873.
(42) Matsuo, T.; Kobayashi, K.; Tago, K. Estimation of the Solubility Dependence of Aluminate Salts of Alkali Metals on Ion Radii of Alkali Metals by LDF Molecular Orbital Calculations. *J. Phys. Chem.* **1996**, *100*, 6531−6542.
(43) Drexler, C. I.; Miller, T. C.; Rogers, B. A.; Li, Y. C.; Daly, C. A.; Yang, T.; Corcelli, S. A.; Cremer, P. S. Counter Cations Affect Transport in Aqueous Hydroxide Solutions with Ion Specificity. *J. Am. Chem. Soc.* **2019**, *141*, 6930−6936.
(44) Sipos, P. M.; Hefter, G.; May, P. M. Viscosities and Densities of Highly Concentrated Aqueous MOH Solutions ($M^+ = Na^+$, $K^+$, $Li^+$, $Cs^+$, $(CH_3)_4N^+$) at 25.0°C. *J. Chem. Eng. Data* **2000**, *45*, 613−617.
(45) Kraus, H.; Müller, M.; Prins, R.; Kentgens, A. P. M. Comments on the $^{27}$Al NMR Visibility of Aluminas. *J. Phys. Chem. B* **1998**, *102*, 3862−3865.
(46) Pushparaj, S. S. C.; Forano, C.; Prevot, V.; Lipton, A. S.; Rees, G. J.; Hanna, J. V.; Nielsen, U. G. How the Method of Synthesis Governs the Local and Global Structure of Zinc Aluminum Layered Double Hydroxides. *J. Phys. Chem. C* **2015**, *119*, 27695−27707.
(47) Di Bitetto, A.; André, E.; Carteret, C.; Durand, P.; Kervern, G. Probing the Dynamics of Layered Double Hydroxides by Solid-State $^{27}$Al NMR Spectroscopy. *J. Phys. Chem. C* **2017**, *121*, 7276−7281.
(48) Britto, S.; Kamath, P. V. Structural Synthon Approach to the Study of Stacking Faults in the Layered Double Hydroxides of Lithium and Aluminum. *Z. Anorg. Allg. Chem.* **2012**, *638*, 362−365.
(49) Hou, X.; Kirkpatrick, R. J. Thermal Evolution of the $Cl^-$−$LiAl_2$ Layered Double Hydroxide: A Multinuclear MAS NMR and XRD Perspective. *Inorg. Chem.* **2001**, *40*, 6397−6404.
(50) Vijayakumar, M.; Kerisit, S.; Yang, Z.; Graff, G. L.; Liu, J.; Sears, J. a; Burton, S. D.; Rosso, K. M.; Hu, J. Combined $^{6,7}$Li NMR and Molecular Dynamics Study of Li Diffusion in $Li_2TiO_3$. *J. Phys. Chem. C* **2009**, *113*, 20108−20116.
(51) McWhinney, H. G.; James, W. D.; Schweikert, E. A.; Williams, J. R.; Hollenberg, G.; Welsh, J.; Sereatan, W. Diffusion of Lithium-6 Isotopes in Lithium Aluminate Ceramics Using Neutron Depth Profiling. *J. Nucl. Mater.* **1993**, *203*, 43−49.
(52) Rahn, J.; Witt, E.; Heitjans, P.; Schmidt, H. Lithium Diffusion in Ion-Beam Sputtered Amorphous $LiAlO_2$. *Z. Phys. Chem.* **2015**, *229*, 1341−1350.
(53) Van Der Ven, A.; Bhattacharya, J.; Belak, A. A. Understanding Li Diffusion in Li- Intercalation Compounds. *Acc. Chem. Res.* **2013**, *46*, 1216−1225.
(54) Tsuneishi, T.; Sakamoto, H.; Hayashi, K.; Kawamura, G.; Muto, H.; Matsuda, A. Preparation of Hydroxide Ion Conductive KOH−layered Double Hydroxide Electrolytes for an All-Solid-State Iron−air Secondary Battery. *J. Asian Ceram. Soc.* **2014**, *2*, 165−168.
(55) Chen, M.; Shen, W.; Lu, X.; Zhu, R.; He, H.; Zhu, J. Jumping Diffusion of Water Intercalated in Layered Double Hydroxides. *J. Phys. Chem. C* **2016**, *120*, 12924−12931.
(56) Staal, L. B.; Charan Pushparaj, S. S.; Forano, C.; Prevot, V.; Ravnsbæk, D. B.; Bjerring, M.; Nielsen, U. G. Competitive Reactions during Synthesis of Zinc Aluminum Layered Double Hydroxides by Thermal Hydrolysis of Urea. *J. Mater. Chem. A* **2017**, *5*, 21795−21806.
(57) Zhang, X.; Huestis, P. L.; Pearce, C. I.; Hu, J. Z.; Page, K.; Anovitz, L. M.; Aleksandrov, A. B.; Prange, M. P.; Kerisit, S.; Bowden,


DOI: 10.1021/acs.inorgchem.9b02000
*Inorg. Chem.* 2019, 58, 12385−12394

M. E.; et al. Boehmite and Gibbsite Nanoplates for the Synthesis of Advanced Alumina Products. *ACS Appl. Nano Mater.* **2018**, *1*, 7115−7128.
(58) Vyalikh, A.; Zesewitz, K.; Scheler, U. Hydrogen Bonds and Local Symmetry in the Crystal Structure of Gibbsite. *Magn. Reson. Chem.* **2010**, *48*, 877−881.
(59) Cadars, S.; Layrac, G.; Gerardin, C.; Deschamps, M.; Yates, J. R.; Tichit, D.; Massiot, D. Identification and Quantification of Defects in the Cation Ordering in Mg/Al Layered Double Hydroxides. *Chem. Mater.* **2011**, *23*, 2821−2831.
(60) Hu, J. Z.; Zhang, X.; Jaegers, N. R.; Wan, C.; Graham, T. R.; Hu, M.; Pearce, C. I.; Felmy, A. R.; Clark, S. B.; Rosso, K. M. Transitions in Al Coordination during Gibbsite Crystallization Using High-Field $^{27}$Al and $^{23}$Na MAS NMR Spectroscopy. *J. Phys. Chem. C* **2017**, *121*, 27555−27562.
(61) Delmas, C.; Maccario, M.; Croguennec, L.; Le Cras, F.; Weill, F. Lithium Deintercalation in $LiFePO_4$ Nanoparticles via a Domino-Cascade Model. *Nat. Mater.* **2008**, *7*, 665−671.
(62) Shen, Z.; Kerisit, S. N.; Stack, A. G.; Rosso, K. M. Free-Energy Landscape of the Dissolution of Gibbsite at High pH. *J. Phys. Chem. Lett.* **2018**, *9*, 1809−1814.
(63) Xu, B.; Qian, D.; Wang, Z.; Meng, Y. S. Recent Progress in Cathode Materials Research for Advanced Lithium Ion Batteries. *Mater. Sci. Eng., R* **2012**, *73*, 51−65.



DOI: 10.1021/acs.inorgchem.9b02000
*Inorg. Chem.* 2019, 58, 12385−12394